

Final Draft
of the original manuscript:

Froend, M.; Riekehr, S.; Kashaev, N.; Klusemann, B.; Enz, J.:
**Process development for wire-based laser metal deposition of 5087
aluminium alloy by using fibre laser.**
In: Journal of Manufacturing Processes. Vol. 34 A (2018) 721 - 732.
First published online by Elsevier: July 26, 2018

DOI: 10.1016/j.jmapro.2018.06.033
<http://dx.doi.org/10.1016/j.jmapro.2018.06.033>

Process development for wire-based laser metal deposition of 5087 aluminium alloy using fiber laser

Authors: M. Froend^{1,2}, S. Riekehr², N. Kashaev², B. Klusemann^{1,2}, J. Enz²

Affiliations:

¹*Leuphana University of Lüneburg, Institute of Product and Process Innovation, Volgershall 1, D-21339 Lüneburg, Germany*

²*Helmholtz-Zentrum Geesthacht, Institute of Materials Research, Department of Joining and Assessment, Max-Planck-Straße 1, 21052 Geesthacht, Germany;*

Corresponding author: M. Froend, Tel.: +49-4152-87-2558, E-mail: martin.froend@hzg.de

Abstract

In the last decades, laser metal deposition (LMD) as a part of additive manufacturing developed to a state of the art methodology in industrial fields. In recent years, there has been an increased interest in the processability of lightweight high strength structural materials such as aluminium alloys. However, in terms of wire-based LMD there is a lack of knowledge regarding the possibility to process aluminium and its alloys. In this research, a process development for wire-based laser metal deposition of a 5087 aluminium alloy (AlMg4.5MnZ) was conducted. Special attention was paid to investigate effects, which are traced back to the specific process energy, in terms of porosity, microstructure and geometric shape of the structures. It was found that process energies between 125 J/g and 185 J/g in combination with a deposition speed of 5 m/min for deposition rates from 25 g/s to 35 g/s using a pre-heated substrate material at 150°C could achieve 99.9% dense structures. Using this knowledge, surface coating as well as structure building parameter windows are identified, which are considerable different.

Keywords: laser additive manufacturing; aluminium alloy; laser metal deposition; process development, microstructure, process parameter windows;

1. Introduction

From its development in the late 1980s, additive manufacturing (AM) became a profitable method to generate components and structures for industrial use nowadays. The concept of this technique consists in melting a material, usually provided as powder or wire and adding it layer-by-layer to build components instead of a subtractive manufacturing as cutting or milling [1]–[4]. This enables a large degree of freedom from construction point of view but also includes great advantage in terms of the degree of utilisation including an inherent simplicity in building three dimensional shaped parts [5], [6]. In comparison to conventional machining methods, AM leads to a significant decrease of material wastage from 90% up to 7% [7], [8]. Hence, an important cost and cycle time minimization by saving the tool change time per part can be realized [9]. From the economic point of view, fabrication of wire material in contrast to powder is comparably cheap, which is one of the reasons for its beneficial balance of accounts [10].

In the field of additive manufacturing, many different approaches have been developed over the last decades. Regarding the production of metallic parts, these approaches can be divided in powder and wire-based techniques [11]. Powder-based approaches have already achieved a significant application in several industrial fields [12]. Powder-based approaches are subdivided in powder bed and powder-feeding techniques [13]. In case of powder bed systems, a certain amount of pulverized metallic material is supplied in a machining chamber, which is flooded by shielding gas. This powder material is irradiated locally by a laser beam, which is led across the powder bed following a predefined path according to the computational design [14]. After solidification of the molten material, a following layer of powder material is automatically put on top of the manufactured structure. This method is repeated until the desired shape of the workpiece is manufactured.

In contrast to this, in powder injection approaches the pulverized material is supplied through a nozzle on the workpiece where it is molten by a laser beam in order to produce the desired shape of the workpiece. At this juncture, an inherent gas such as argon or helium is used to blow the pulverized material on the workpiece, simultaneously protecting the melting pool of reacting with atmospheric gases.

Similar to this, within the wire-based approaches the wire is fed through a nozzle on to workpiece. Using this technique the desired structure is also manufactured by adding certain layers of material on top of or next to each other. Similar to powder-feeding approaches, the material is shielded by an inherited gas during the molten state. However, the surface area of the injected wire using wire-based AM is much lower than the accumulated surface area of the powder particles in powder-based approaches, which reduces the hazard of possible reactions with atmospheric gases during molten state. Therefore, it is not necessary to work in a closed area of inherited gas, which increases the degree of freedom for the approach drastically. AM using wire feeding systems, compared to powder-feeding systems offers higher usage efficiency of material [15], improved surface quality of the deposited structures [3], [10], and enables higher disposition rates [3]. This underlines the necessity of deeper investigations of wire-based LMD.

In general, the application of AM can be divided into a structure building and a surface coating approach. For each purpose, specific process adjustments have to be considered to achieve the desired properties of the workpiece. A high deposition rate and low penetration depths are beneficial in terms of manufacturing structures, whereas a higher penetration into the substrate material is required in case of surface coatings. In both cases, the deposited layer requires strong metallurgical bonding with the substrate material and a very localized heat affected zone [16]–[18], which stresses its applicability for the production of dense parts.

In the following, an AM technique using filler wire as raw material and laser as energy input is investigated. This approach offers very high deposition rates in a well controllable process [18], [19]. Local shielding in the melting zone instead of a shielding gas flooded working area, as it is needed for powder deposition methods, could be applied in wire-based LMD. Because of the variegated adaptability in industrial fields, a process development addressing the identification of high impact parameters in LMD of the aluminium alloy 5087 for a surface coating and structure building process, with special attention to macro-morphology, is investigated. Therefore, a parametric study including the examination of possible defects and outer appearance of the specimens is conducted.

Within AM, the minimization of post-processing is one of the most important factors [18]. In the field of surface coating, mostly milling to straighten the surface roughness is conducted. This results in a certain amount of waste material, which was removed. In order to reduce this amount of waste material and simultaneously to minimize post-processing steps, near net shaped workpieces have to be manufactured. For this purpose, the defined process windows have to be configured precisely in such a way that a high efficiency whether for coating or structure building application can be achieved. Within this study, a process development in order to enable the processability of the aluminium alloy 5087 for LMD was conducted.

2. Laser metal deposition using filler wire

2.1. Materials

In this study, the aluminium alloy AlMg4.5MnZr (EN AW-5087) as wire-material and AlMg3 (EN AW-5754) as substrate-material were investigated. The 5xxx series are characterized as the stiffest in the area of the non-thermosetting aluminium alloys and as good weldable in laser beam welding (LBW) processes [20]. The wire was provided with a diameter of 1.0 mm and speed controlled fed through a nozzle on to workpiece. The substrate material was provided as 200 mm x 150 mm rolled sheets with 6 mm thickness. The deposition direction was adjusted to the rolling direction of the substrate material. Due to the high reflectivity of aluminium and furthermore to clean the upper layer of the substrate material, the substrate was firstly sandblasted and cleaned with acetone before LMD. A pressure of 8 bar and a particle size of 90 μm – 150 μm of the blasting material were used to achieve a surface roughness of $R_a = 0.20 \mu\text{m}$ and $R_z = 1.36 \mu\text{m}$.

2.2. Process development

An 8 kW continuous wave ytterbium fiber laser YLS-8000-S2-Y12 (IPG Photonics Corporation) integrated with an optical head YW52 Precitec, in a CNC-supported XYZ-machining center (IXION Corporation), was employed in this study. The main characteristics of the laser and the characteristic features of the focused beam are shown in Fig. 1 and summarized in Table 1. The optical head was integrated along the Z-axis of the system, which was also equipped with a wire feeding system together with a shielding gas supply, as schematically illustrated in Fig. 2. Within the LMD process, relative to the manufactured design of the workpiece, the laser locally heats up the substrate. Due to this, temperature gradients leading to internal residual stresses occur. Hence, plastic deformation of the substrate as well as in the deposited structure develops [21]. This effect is known as temperature gradient mechanism [22]–[25]. In AM distortions of the workpiece are a critical problem which have to be minimized by adjusting the optimum parameter window fitted to the specific shape of the workpiece [22], [25]–[28]. To reduce distortions the substrate was pre-heated to different temperatures in order to provide a more homogenous heat profile within the substrate and the deposited structure. For this purpose, the substrate was clamped on an IKA C-MAG HS7 heating plate with a maximum power of 1 kW (maximum temperature 500°C). Equally important is that pre-heating of the substrate reduces internal defects like porosity or cracking [29].

During the process, the wire was fed through a nozzle at a fixed angle of 35° relative to the surface of the substrate. The nozzle for the shielding gas supply was installed above the wire nozzle with an angle of 55°, a vertical distance of 25 mm, and a horizontal spacing of 5 mm relative to the front edge of the wire feeding nozzle. The amount of shielding gas was adjusted to 13 l/min in order to provide enough gas to protect the molten material from oxidation with atmospheric gases but not to influence the solidification process. Due to the high viscosity of aluminium in its liquid state together with a very high cooling rate within the LMD process, the shape of the deposited structure could be distorted using a too strong gas flow. As an alternative, the deposition could be conducted in a complete shielding gas atmosphere, like an argon-filled chamber. However, this approach is less adaptable within industrial application due to geometric restrictions. Therefore, the process was adjusted using local shielding to increase the degree of freedom with respect to possible dimensions of the workpiece. The circular shaped laser beam irradiates the wire perpendicular to the substrate. Due to the fact that the wire is supplied on a wound up coil, it develops an inherent drill which could affect the feeding accuracy by an oscillating movement after leaving the nozzle. Considering this, the spot diameter was enhanced to 1.6 mm by a positive defocusing to + 23 mm for building multiple layer structures but keeping the process energy, constant. Adjusting the laser spot size could provide a homogeneous melting of the wire in each oscillated position and simultaneously melt the surface of the substrate to merge the materials in LMD. In Fig. 1 (a) and (b) the beam caustic for the used equipment is visualized. Additionally, the beam intensity for focal position (c) as well as for Rayleigh length (d) is plotted. From this, it can clearly be seen that a top hat distribution is achieved using focal position, whereas a gaussian distribution shape is formed in Rayleigh length. Therefore, it can be concluded that the enhancement of the spot diameter provides a sufficient beam intensity to melt the wire. Additionally, neighboured regions of the subjacent substrate or structure are heated up in order to achieve homogeneous heat distributions in the manufacturing zone and to balance oscillations of the wire. Furthermore, possible astigmatism was balanced by the adjustment of the equipment and a linear deposition path. For more complex structures which require also curved, or circularly paths, astigmatic effects have to be taken into account. In this study only straight-lined beads were deposited. The distance

between the focal spot and the edge of the wire feeding nozzle was adjusted to be as small as possible, in order to reduce oscillating movements of the wire and improve process accuracy. Regarding this, the distance of $d_N = 4$ mm could be defined as a minimum to ensure that the edge of the wire nozzle was not melted during the process. Additionally, this distance is large enough to avoid remaining not molten material located on the nozzle after switching off the laser. Otherwise, this remaining material, might be remolten starting the deposition of the next bead and drop on the substrate leading to defects. The same effect occurs for the process-related development of smoulder which accumulates at the notch too. Within the process, the table of the CNC-system was moved relatively to the Z-axis in X or Y direction with a defined velocity v_t . At the same time, the wire material was fed through the nozzle with a velocity v_w . Using the presented process, it is possible to deposit lines of AA5087 on the substrate and to regulate the deposition rate by adjusting the ratio between v_t and v_w . This ratio is expressed as $v_w/v_t = k$ in what follows.

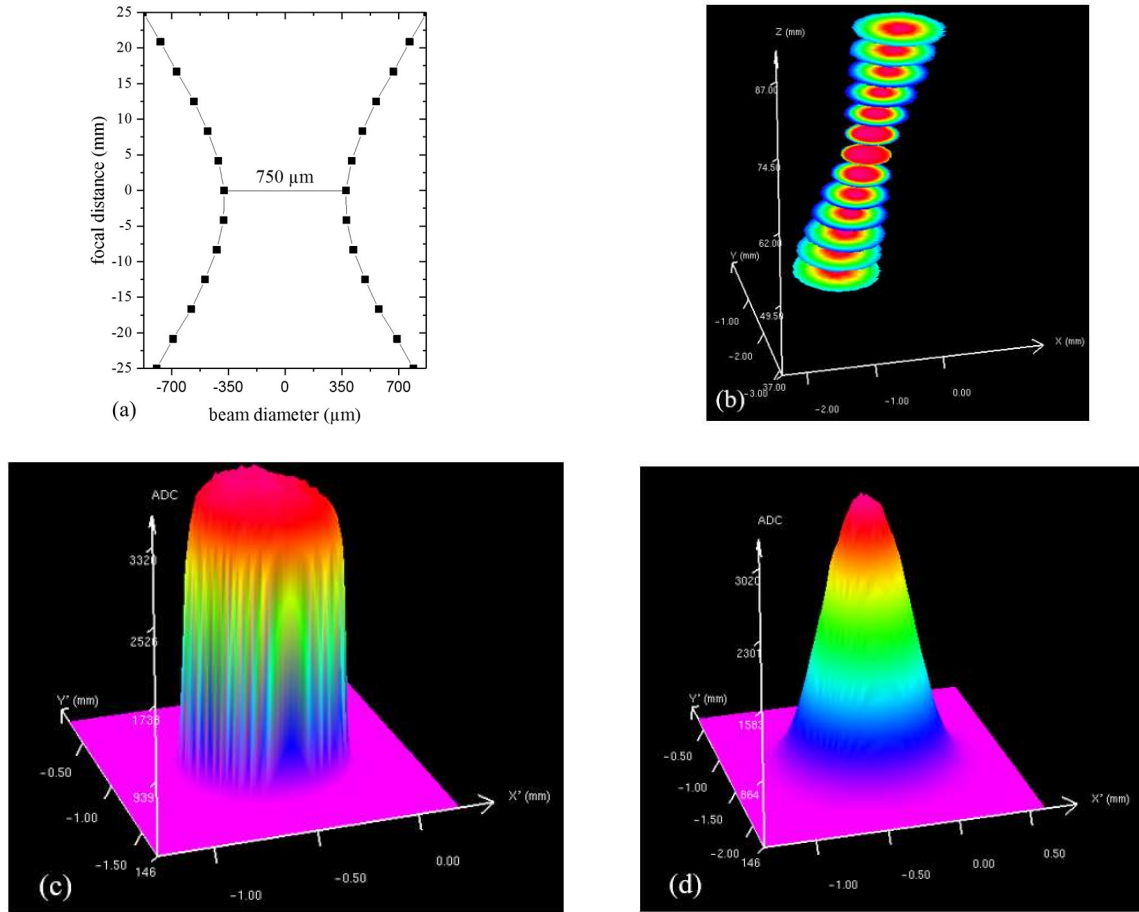


Fig. 1 Overview of the beam caustic (a), beam symmetry (b) and beam intensity distribution in focal (c) and Rayleigh length position (d) showing a top-hat distribution in focal position and a gaussian-shaped distribution at Rayleigh length.

Table 1: Main properties of the laser equipment

parameter	symbol	value	unit
maximum power	P_{\max}	8000	W
collimation lens	L_C	120	mm
focal lens	F	300	mm
process fiber diameter	D	300	μm
focal spot diameter	d_f	750	μm
center wavelength	λ	1070	nm
divergence half-angle	$\theta/2$	30.35	mrad
beam parameter product	BPP	9.9	mm · mrad
beam quality factor	M^2	29	-
rayleigh length	Z_r	12.3	mm

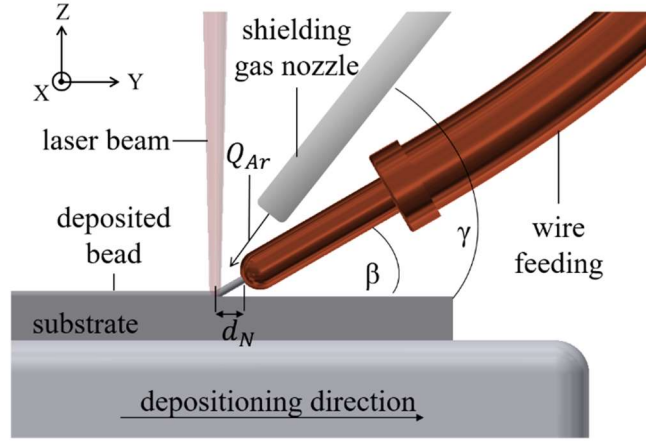


Fig. 2: Schematic visualization of the LMD process showing also the identification of the fixed parameters: flow rate of shielding gas Q_{Ar} , the shielding gas nozzle angle γ , the wire feeding nozzle angle β , the focal spot to wire feeding nozzle tip distance d_N as well as the deposition direction.

Parameter dependent bead shapes with height H and width ω were produced, as shown in Fig. 3(a). As a result of the dynamic process wire and substrate partly diluted inside the substrate, which is expressed by the dilution depth h . Hence, the created bead is welded into the substrate expressed in a high bonding between build-up structure and the substrate or between multiple layers [18], [30]–[32]. Relative to the chosen parameters and the resulting process energy, the bead width, dilution depth and bead height vary [33]. As an indicator for the ratio between the width and height of the bead, the bead side angle α and the height-to-width ratio R_B , were defined [34]. The general bead shape is visualized in Fig. 3 (a). In addition to that two different possibilities of LMD with multiple layers next to each other or on top of each other are sketched in Fig. 3 (b) and (c), respectively in the following, an experimental study to characterize the resulting bead shape, inner defects, dilution and overlapping ratios depending on varied process parameters, is presented.

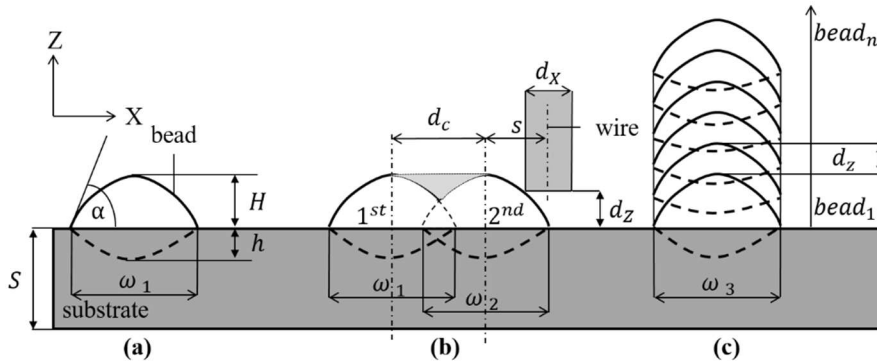


Fig. 3: Identified geometric parameters for bead morphologies after LMD for single beads (a), multiple beads next to each other (b) [33] or multiple beads on top of each other (c).

3. Theory

Within the LMD process, numerous parameters have to be adjusted in order to define quantifiable input values. Additionally, the process with respect to the chosen input has been evaluated. Therefore, the following theoretical equations and assumptions have been derived.

3.1. Adjustment of the laser specific parameters

Using deposition velocity v_t within the process time t , it is possible to determine a deposited line length l . This is expressed as

$$l = v_t t. \quad (3.1)$$

By this, it is clear that the achieved length of the bead is only dependent on the deposition velocity with respect to the process time and independent from the wire feeding rate. However, the deposited volume of the bead V varies with the wire feeding velocity v_w as

$$V = v_w \pi r^2 t, \quad (3.2)$$

where r is the radius of the wire. Additionally, the deposition rate \dot{V} as an important indicator of the deposited material is expressed as

$$\dot{V} = v_w \pi r^2 \rho, \quad (3.3)$$

where ρ is the density of the material. The mass of the deposited bead equals

$$m = v_w \pi r^2 \rho t. \quad (3.4)$$

Within laser beam welding an energy parameter, namely fluency, which expresses the laser power for an irradiated area, is used. The third dimension to create voluminous parts has also to be considered. Therefore, the specific energy per unit volume of wire W , as an extension of the common used fluency is expressed as

$$W_{mm^3} = \frac{dE}{dV} = \frac{P}{v_w \pi r^2} \quad (3.5)$$

or

$$W_g = \frac{dE}{dm} = \frac{P}{v_w \pi r^2 \rho}. \quad (3.6)$$

The cross section of the bead S is expressed by the ratio of volume to length

$$S = \frac{V}{l} = \frac{v_w \pi r^2}{v_t}. \quad (3.7)$$

In order to generate a defined irradiated area of the circular shaped laser beam, it is possible to adjust the focal diameter by positioning the optical head relatively to the surface of the substrate. Hence, the focal spot diameter is described by Equation (3.8) as a ratio between the so-called Rayleigh length z_r and the defocussing distance in Z-direction abbreviated by z , relatively to the equipment specific smallest focal spot diameter d_f as

$$d(z) = d_f \sqrt{1 + \left(\frac{z}{z_r}\right)^2}. \quad (3.8)$$

3.2. Geometric examination of the beads

As already mentioned, LMD processes are used to build structures or coat surfaces. In order to be able to adjust the surface quality in coating processes it was assumed in [35] that the geometry of the resulting beads can be considered as circularly shaped. This is visualized in Fig. 4 (a). Consequently, the radius R of the deposited bead is calculated by considering the deposited height and width of the bead. In case of a multiple layer process next to each other, bead spacing has to be defined. As shown in Fig. 4 (b) it can be derived that the center of the first bead is located at $(0, H - R)$. Also referring to [35], the circle can be expressed as

$$R^2 = [Z - (H - R)]^2 + x^2, \quad (3.9)$$

where

$$R = \frac{\left(\frac{\omega^2}{4 + H^2}\right)}{2H}. \quad (3.10)$$

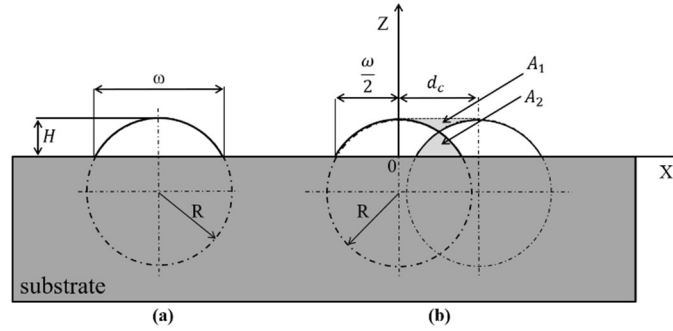


Fig. 4: Geometric assumptions for bead and molten zone geometries as circularly shaped with defined parameters according to [35].

In order to get the smoothest surface for multiple LMD in coating processes, the areas A_1 and A_2 have to be equal. Only in this case, the surface transition between the neighboured beads is close to being plane. When $X > 0$, areas A_1 and A_2 can be calculated by reformulating Equation (3.9) as:

$$Z = f(x) = \sqrt{R^2 - x^2} + (H - R). \quad (3.11)$$

Using these relations, the two areas A_1 and A_2 , as indicated in Fig. 4 (b) can be calculated by integration method given as:

$$\begin{aligned} A_1 &= H \cdot d_c - 2 \int_0^{\frac{d_c}{2}} \left(\sqrt{R^2 - x^2} + H - d_c \right) dx \\ &= R \cdot d_c - R^2 \sin^{-1} \left(\frac{d_c}{2R} \right) - \frac{d_c}{2} \sqrt{\left(R^2 - \left(\frac{d_c}{2} \right)^2 \right)}, \end{aligned} \quad (3.12)$$

and

$$\begin{aligned}
A_2 &= 2 \int_{\frac{d_c}{2}}^{\frac{\omega}{2}} (\sqrt{R^2 - x^2} + H - d_c) dx \\
&= \left[R^2 \sin^{-1} \left(\frac{\omega}{2R} \right) - \frac{\omega}{2} \sqrt{R^2 - \left(\frac{\omega}{2} \right)^2} \right] \\
&\quad - \left[R^2 \sin^{-1} \left(\frac{d_c}{2R} \right) - \frac{d_c}{2} \sqrt{R^2 - \left(\frac{d_c}{2} \right)^2} \right] + (H - R)(\omega - d_c).
\end{aligned} \tag{3.13}$$

Additionally, [35] described the overlapping ratio of the beads, given as

$$\mu_c = \frac{(\omega - d_c)}{\omega}. \tag{3.14}$$

As formerly stated, the beads are welded into the substrate, which causes a high bonding. Due to different irradiation times relative to the specific process energy, different dilution ratios occur. As in [36] already stated, the dilution is “the variation degree of composition of cladding arising from the blend of molten substrate during the laser cladding”. Assuming a circularly geometric shape of the bead as well as for the molten zone, the dilution is expressed as

$$\eta = \frac{\left[\frac{\left(\left(\frac{\omega}{2} \right)^2 + h^2 \right)^2}{h\omega} \sin^{-1} \left(\frac{h\omega}{\left(\frac{\omega}{2} \right)^2 + h^2} \right) - \left(\left(\frac{\omega}{2} \right)^2 - h^2 \right) \right]}{\frac{h \left(\left(\frac{\omega}{2} \right)^2 + H^2 \right)^2}{\omega H^2} \sin^{-1} \left(\frac{H\omega}{\left(\frac{\omega}{2} \right)^2 + H^2} \right) + \frac{\left(\left(\frac{\omega}{2} \right)^2 - h^2 \right)}{h\omega} \sin^{-1} \left(\frac{h\omega}{\left(\frac{\omega}{2} \right)^2 + h^2} \right) - \frac{\left(\left(\frac{\omega}{2} \right)^2 - Hh \right) (H + h)}{H}}. \tag{3.15}$$

Taking the different maxima of dilution and bead height into account, the dilution ratio can be simplified to

$$\eta_{max} = \frac{h}{(h + H)}. \tag{3.16}$$

To express a relation between bead height and bead width the so-called aspect ratio R_B of the bead is defined as

$$R_B = \frac{H}{\omega}. \tag{3.17}$$

Additionally the ratio between the deposition height and dilution depth is calculated as

$$R_C = \frac{H}{h}. \tag{3.18}$$

Within the representation and discussion of the results, these equations are used to calculate the dilution ratios and identify adaptable process parameters according to qualitative requirements defined in section 4.

During LMD, residual stresses due to shrinkage effects may develop [24], [37]–[39]. Fig. 5 depicts the possible reasons for residual stresses within the deposited structures. It is assumed that due to shrinkage effects of the deposited beads internally compressive stresses occur [40]. During the process, a bead of the length l_{hot} is deposited, Fig. 5 (a), and contracts while solidification to the length l_{cool} , Fig.5 (b). Because of the strong bonding between the substrate material and the deposited bead, compressive stresses in the substrate occur. These stresses may induce distortions of the structure in X-Z direction, which are shown in Fig.5 (b) to (d). Fig. 5 (d) also visualizes the deposition of a second bead on top, where the same effect occurs again. This leads to compressive stresses in

the first bead and substrate which additionally increases the development of a distortion angle φ_1 . Due to the so-called temperature gradient effect, additional distortions in Y-Z directions occur. By this mechanism, depicted in Fig. 5 (e), also internal residual stresses develop, which may lead to a large enough internal moment to deform the material by a distortion angle φ_2 [41], [42]. In the parametric study, pre-heating of the substrate is used to reduce distortion effects. Additionally, cracking inside the bead, Fig. 5 (f), can occur, which needs also to be analysed with respect to the process parameters.

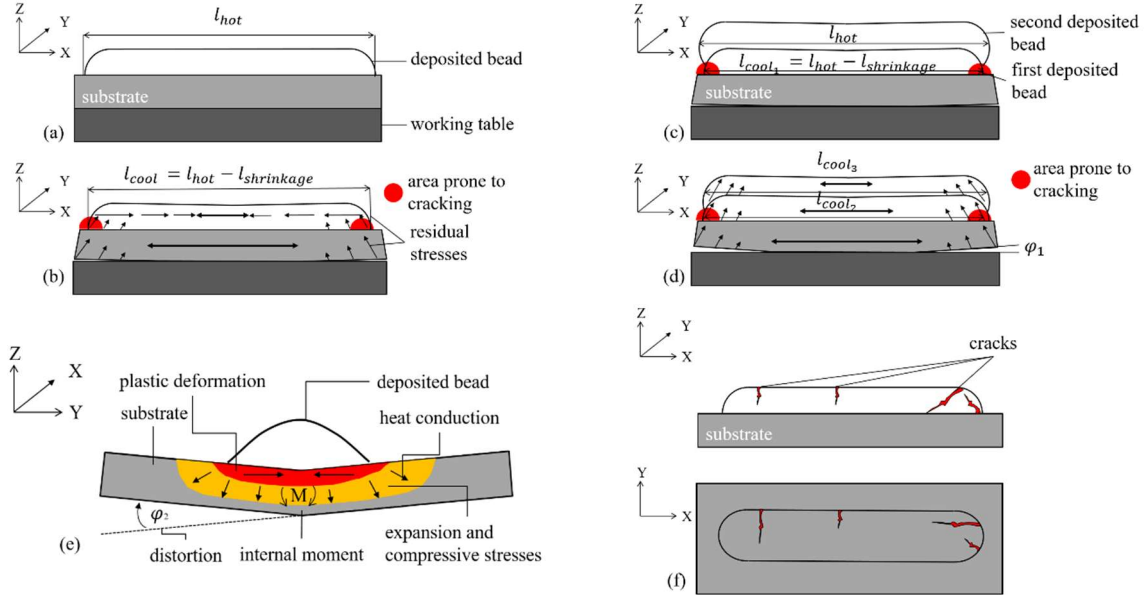


Fig. 5: Schematic visualization of a deposited bead with a length of l_{hot} (a) and its shrinkage while cooling down inducing residual stresses and deformations of the substrate for a single bead deposition (b) and (e). As well as multiple layer LMD with bead lengths of l_{hot} due to subsequent deposition (c) and cooled down state which leads to residual stresses in both layers and the substrate (d). Additionally, cracking within the bead is visualized (f).

4. Parametric study

For the process of LMD, many important parameters, depicted in Fig. 2, 3 and 4, are identified. They affect the shape and quality of the produced structures, consequently their influence needs to be analysed. Table 2 provides an overview of all varied parameters within this study to gain a global understanding of the process.

Firstly, the positioning of the wire relative to the surface of the substrate was analysed. The tilting angle of the wire feeding nozzle was fixed to 35° . The initial temperature of the substrate was varied between 25°C , 150°C and 300°C . As already mentioned in [29], pre-heating of the substrate reduces porosity and cracking. Additionally, in [3], [43] and [44] were stated that constant process conditions regarding material supply and temperature distributions are needed in order to reduce porosity. Furthermore, heat induced distortions are assumed to decrease using a pre-heated substrate material due to minimizing the temperature gradient within the process.

To identify the Z-directional tolerance within the process, a bead with a wire position of $Z = 0.0$ mm relatively to the surface was deposited. Moreover, the positioning was varied in $Z = + 0.1$ mm steps producing single beads until the identification of the upper borders of losing penetration. This information is of great importance preventing in case of unstable deposition heights within one bead, due to temperature related effects or distortions of the substrate, the process to become unstable.

Secondly, based on the defined optimal wire-positioning, parameter variations of power, deposition and wire velocity were investigated. Based on this systematic study, a general understanding of their syndetic dependencies will be identified. For this purpose, common characteristic factors in AM like the k-factor, expressed as the deposition rate, as well as the specific process energy W per deposited volume, expressing the energy to k-factor, were applied. The produced samples using k-factors varying from 1 to 10 in connection with a variation of the power from $P = 3500$ W - 4500 W were examined by X-ray analysis. The pores within the structure are assumed

to be spherical. Using X-ray analyses, pore diameters were measured and the relative volume of pores within one deposited bead was calculated. The density of the bead ρ_{bead} is expressed as

$$\rho_{bead} = v_w \pi r^2 t - \sum_{i=1}^n V_{pore_i}, \quad (4.1)$$

with

$$V_{pore_i} = \frac{\pi d_{pore}^3}{6}, \quad (4.2)$$

where d_{pore} is the diameter of each individual pore.

Thirdly, geometric shape properties like the bead height, width, side angle and penetration depth were analysed. Especially in the case of dividing the LMD process into structure building and surface coating aimed applications, different parameter windows have to be defined for each purpose, in order to comply the application requirements. Therefore, the characterization of the dilution ratio of the bead and the substrate has to be considered. Hence, the metallurgical bonding with the substrate as a result of the chosen process parameters can be identified. Specifically in case of surface coating application, the overlapping ratio, indicated in Fig. 4 (b) and predominantly determined by an adjustment of the bead spacing d_c , has to be considered. To examine the resulting surface roughness for the estimated values of d_c , four different bead distances, ranging from 4.1 mm to 2.15 mm on two different pre-heated substrates of 150°C and 300°C were used.

To characterize the shape of the deposited beads several assessment criteria were defined. In terms of constant processability, a homogenous bead shape is needed. A homogenous shape is defined by low surface roughness and a constant width along the bead. Fig. 6 (a) and (b) depict homogenous bead shapes with constant height and width along the bead. Fig. 6 (c) and (d) indicate possible shape instabilities like different bead widths ω_1 and ω_2 , varying widths $\Delta\omega$, along the bead, different bead heights between the start and end points H_1 and H_2 and increased surface roughness ΔH due to a varying height along the bead. Additionally, regarding structure building LMD a bead spacing $d_c = 0$ and consequently a tilting angle $\delta = 0$ is required in order to produce Z-directional structures with no over overhang. This effect is illustrated in Fig. 7 (a) and (b).

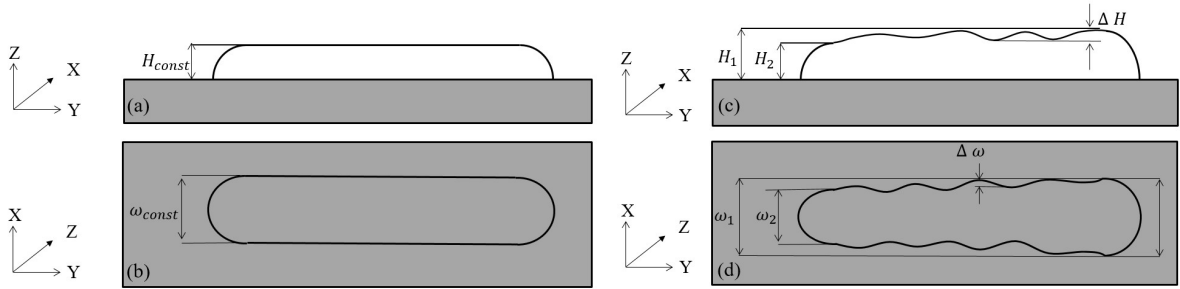


Fig. 6: Target shapes considering constant height (a), width (b) for single beads as well as varying height (c) and width (d) within one bead as deficient product criterias.

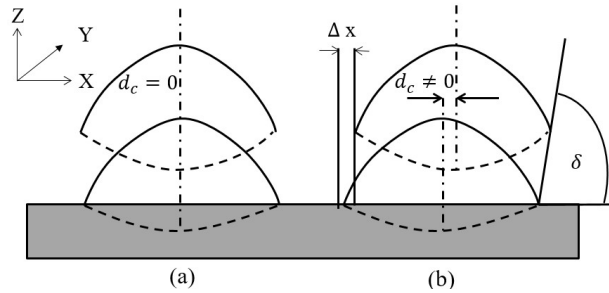


Fig. 7: Optimal positioning for multiple layer LMD (a) and a resulting tilting angle δ in case of $d_c \neq 0$ (b).

Table 2: Overview of varied process parameters

parameter	symbol	parameter variation	unit
laser power	P	3500, 4000, 4500	W
deposition velocity	v_t	16.67, 33.34, 50, 66.67, 83.34	mm/s
wire velocity	v_w	16.67, 33.34, 50, 66.67, 83.34, 100, 116.67, 133.34, 150, 166.67	mm/s
focus spot diameter	d_f	0.75, 1.6	mm
Z-directional wire offset	d_w	0, 0.1, 0.2, 0.3	mm
substrate temperature	T_s	25, 150, 300	°C

5. Results and discussion

5.1. Macro-morphologies and visual inspection

Within the experimental study it was detected that a laser power minimum of 3500 W has to be used in order to deposit beads on a substrate with $T_s = 25^\circ\text{C}$ and a deposition velocity of 1 m/min. For pre-heated substrates of 150°C and 300°C , the laser power had to be increased to 4000 W.

To identify the Z-directional tolerance of the process, beads with a length of $l = 100$ mm were deposited. The results, summarized in Table 3, indicate a maximum possible distance between the wire tip and substrate surface of $Z = + 0.3$ mm for substrate material at room temperature. This value indicated the maximum Z-directional distance tolerance between substrate and wire tip for $T_s = 25^\circ\text{C}$. This tolerance decreased to $Z = + 0.1$ mm in the case of a substrate temperature of 150°C and 300°C . It follows, that low substrate temperatures provide a higher Z-directional wire-positioning tolerance in terms of a stable deposition process.

In structure building LMD, the structure is heated up for each additional bead. This results in a high process temperature. Therefore, it is concluded that the Z-directional wire-positioning has to be of high precision for a stable LMD process, not exceeding $Z = + 0.1$ mm. Within the parametric study, an offset of $Z = 0$ mm was used.

Table 3: Results of the experimental study in order to find the maximum possible distance between substrate and wire tip for different substrate temperatures

Z-directional wire offset	substrate temperature		
	25°C	150°C	300°C
+ 0.4 mm	no connection	no connection	no connection
+ 0.3 mm	connection	no connection	no connection
+ 0.2 mm	connection	no connection	no connection
+ 0.1 mm	connection	connection	connection
0 mm	connection	connection	connection

Investigations regarding the bead shape relative to the substrate temperature were also conducted. It was detected, that the shape for beads deposited on substrate material at room temperature of 25°C is more irregular, resulting in varying bead heights within one bead and inhomogeneous connection to the substrate, compared to beads on pre-heated substrate material. The shape variation with respect to different substrate temperatures is shown in Fig. 8 (a) for a substrate at room temperature, (b) for a pre-heated substrate of 150°C and (c) for a substrate temperature of 300°C . Deposited beads on a substrate at 150°C are constantly shaped and connected to the substrate. This also holds for beads deposited on a pre-heated substrate of 300°C . Indeed, the difference in terms of bead shape from 150°C to 300°C is negligible. These results lead to the conclusion that it is sufficient to use a pre-heating to 150°C to obtain homogenous bead shapes. Additionally, it is concluded that an increased process temperature to 300°C does not decrease the surface quality of the structures.

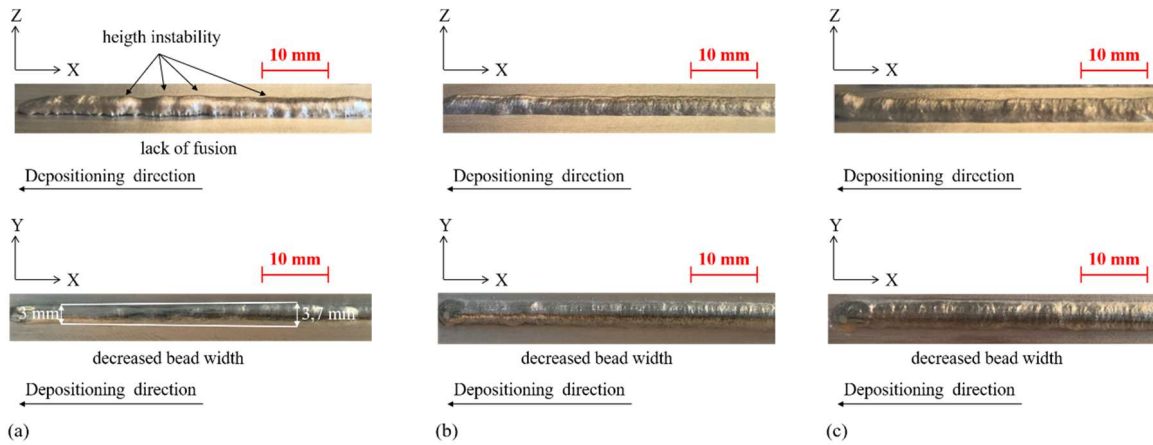


Fig. 8: Bead shape deviations resulting from different substrate temperatures $T_s = 25^\circ\text{C}$ (a), $T_s = 150^\circ\text{C}$ (b), $T_s = 300^\circ\text{C}$ (c) deposited with $P = 4000\text{ W}$, $v_t = 1\text{ m/min}$ and $v_w = 8\text{ m/min}$.

5.2. Radiographic analysis

To detect inner defects of the deposited samples X-ray analyses were conducted. Within this study a Seiferts Isovolt 320/13 X-ray tube using an irradiation angle of 42° , a working distance of 800 mm, a tube voltage of 70 kV and a tube current intensity of 4.2 mA affecting an effective focal spot of 2.25 mm^2 was used. The produced specimens deposited in the parametric study were investigated conforming to EN DIN 35224:2016-02 in order to identify the amount of porosity relatively to the varied parameters.

It needs to be pointed out that the substrate temperature as well as a stable and homogeneous temperature distribution during the LMD process are the dominant requirements to obtain macroscopic defect free structures. The density of the deposited beads within stationary process conditions was elucidated. Therefore, the lead-in and lead-out area, respectively 10 mm each, was not taken into account for the defect analyses. In particular, these regions showed an increased amount of porosity due to process instabilities, elicited by positive and negative accelerations of the machine and injecting of the laser.

Using a substrate temperature at $T_s = 25^\circ\text{C}$, it was possible to deposit beads with a density of $\rho_{bead} = 99.99\%$ using a deposition velocity of $v_t = 1\text{ m/min}$ together with a deposition rate of $\dot{V} = 31\text{ g/s}$ to 35 g/s which expresses a k-factor of 9 and 10. Accordingly, specific process energies of $W_g = 100\text{ J/g}$ and 112 J/g were used. For increased deposition velocities, the process became unstable. Consequently, no beads with a density higher than $\rho_{bead} = 99.90\%$ could be achieved. In case of a pre-heated substrate material at $T_s = 150^\circ\text{C}$ deposited beads with densities more than $\rho_{bead} = 99.99\%$ using $P = (3500, 4000, 4500)\text{ W}$ were possible.

In case of $P = 3500\text{ W}$ a deposition velocity of $v_t = 1\text{ m/min}$ was necessary. Using this velocity, deposition rates of $\dot{V} = 24\text{ g/s}$, 28 g/s and 31 g/s which represent a k-factor from 7 to 9 were used. Consequently, specific energies of $W_g = 112\text{ J/g}$, 126 J/g and 144 J/g were used in the process. Increasing the laser power and deposition velocity to $P = 4000\text{ W}$ and $v_t = 5\text{ m/min}$ also bead densities of more than $\rho_{bead} = 99.99\%$ could be achieved. Furthermore, deposition rates between $\dot{V} = 28\text{ g/s}$ to 31 g/s were necessary to produce the required bead quality. This combination led to specific energies of $W_g = 112\text{ J/g}$, 128 J/g and 144 J/g .

For a laser power of $P = 4500\text{ W}$, dense beads can be produced with a parameter combination of deposition velocities up to $v_w = 5\text{ m/min}$ and deposition rates between $\dot{V} = 21\text{ g/s}$ to 35 g/s , leading to specific energies of $W_g = 130\text{ J/g}$ to 215 J/g . The results, summarized in Table 4, show that a pre-heated substrate is favourable in terms of a reduction of porosity. Additionally, in case of a substrate at room temperature, low deposition velocities, in combination with high deposition rates and laser powers more than $P = 4000\text{ W}$ were needed to obtain a stable process. From these results, it is concluded that high process temperatures are needed to achieve structures that are free from defects. In case of $T_s = 25^\circ\text{C}$, only the deposition velocity of $v_t = 1\text{ m/min}$ was sufficient to result in the required process temperature. In case of pre-heated substrate material, higher deposition velocities and lower laser powers could also achieve bead densities of more than $\rho_{bead} = 99.99\%$ as the pre-heated substrate provides enough temperature to enable a stable process. However, low laser powers of $P = 3500\text{ W}$ were only processable with

deposition velocities of $v_t = 1$ m/min. Using higher deposition velocities, $P = 3500$ W was not sufficient to inject the laser into the material any more.

Table 4: Possible process windows leading to bead densities higher than 99.99%.

parameter set	substrate temperature	laser power	deposition velocity	deposition rate	k-factor	specific energy
# 1	25°C	3500 W	1 m/min	31.3 g/s	9	100.5 J/g
# 2	25°C	3500 W	1 m/min	34.8 g/s	10	111.7 J/g
# 3	25°C	4000 W	1 m/min	34.8 g/s	10	114.9 J/g
# 4	150°C	3500 W	1 m/min	24.3 g/s	7	143.6 J/g
# 5	150°C	3500 W	1 m/min	27.8 g/s	8	125.7 J/g
# 6	150°C	3500 W	1 m/min	31.3 g/s	9	111.7 J/g
# 7	150°C	4000 W	3 m/min	27.8 g/s	2.66	143.6 J/g
# 8	150°C	4000 W	3 m/min	31.2 g/s	3	127.7 J/g
# 9	150°C	4000 W	5 m/min	27.8 g/s	1.6	143.6 J/g
# 10	150°C	4000 W	5 m/min	31.3 g/s	1.8	127.7 J/g
# 11	150°C	4500 W	3 m/min	34.8 g/s	3.33	129.3 J/g
# 12	150°C	4500 W	4 m/min	27.8 g/s	2	161.6 J/g
# 13	150°C	4500 W	4 m/min	31.3 g/s	2.25	143.6 J/g
# 14	150°C	4500 W	5 m/min	24.3 g/s	1.4	184.7 J/g
# 15	150°C	4500 W	5 m/min	27.8 g/s	1.6	161.6 J/g

Additionally, the probability density of porosity averaged over the full parametric study was calculated. The detected pore size showed a maximum diameter of $d_{pore} = 1.2$ mm. Within AM, large pores are very detrimental because the material is weakened. Therefore, a differentiation in size and amount of the pores has to be conducted. Especially in the beginning and in the end of the deposited bead, large pores were found. As can be seen in Fig. 9, the overall average pore size of $d_{pore} = 0.345$ μm was determined. Pore dimensions from 0.24 μm to 0.48 μm appeared with a probability of 68.2%. No dependency between pore size and the varied parameters was observed. In Fig. 9 (b) the cumulative amount of pores is plotted illustrating the probability of occurring pore sizes within the process.

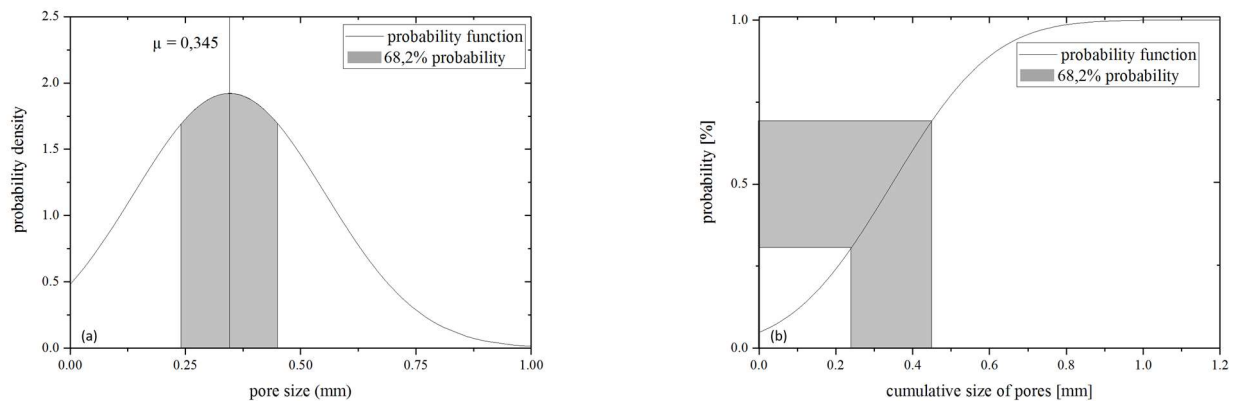


Fig. 9: Probability density (a) and cumulative amount of porosity of the detected porosity (b).

5.3. Metallography and geometric examination

In order to investigate the microstructure and geometric shape of the beads, transverse cross sections from the middle section of the beads were cut. They were mounted, grounded and polished using an oxide polishing suspension compound (OPS). Microstructural observations were performed using an inverted optical microscopy (OM) Leica DMI 5000M with polarized light. Due to its relatively high magnesium content, the material is very corrosion-resistant and consequently common aluminium etching agents are not sufficient to visualize the microstructure. Therefore, an electrolytic etching, using a 2.5%-acidiferous tetrafluoroboric acid causticise (35%) was used. This technique, also known as Barker method was conducted using 30 V and an active reaction time of 90 s.

Fig. 10 shows an overview of the resulting microstructure of one bead, illustrating in particular a Z-directional grain growth, which is typical for LMD processed metallic structures [45], [46]. The general texture of the bead is coarse-grained. Near the top surface, the grains are globular, which can be related to the thermal gradient between the solidifying material and the surrounding atmosphere. Interestingly, a transverse grain growth from the prior deposited into the added bead is observed. During multiple layer LMD, the globular grains in the upper regions are remolten and form the Z-directional grain growth through the transition zone of the beads, plotted in Fig. 11 (a) and (b). In the majority of cases, occurring defects such as pores and cracks are detected in the transition zones between the beads or substrate material, indicated in Fig. 11 (b). The results indicate that the shapes of the pores are circumstantially, like assumed in section 4. Within LMD, cracks are also a challenging problem. It was found that they mostly proceed along the Z-directional grain boundaries, depicted in Figs. 10 and 11, or along the transition zones between the beads or the substrate, see Fig. 11 (b). Crack growth direction is located along the grain boundaries. Within AM, cracking mostly occurs due to high cooling rates and resulting in inhomogeneous temperature fields leading to internal residual stresses. During LMD, a high thermal gradient between the deposited bead and the formerly manufactured structure occurs. As a result residual stresses within the structure may develop, leading to internal defects [25], [38]. Considering high disparities with respect to heat and thermal extension, especially in the start and end areas of the deposited beads, high internal stresses may occur. This effect is also shown in Fig. 5 in which periled areas with high residual stresses were highlighted. The stress concentration in these areas supports crack initiation up to a total separation of bead and substrate material, also known as delamination. Considering this, also cracking along the transition zone of two beads within a structure, depicted in Fig. 11 (b), can be explained.

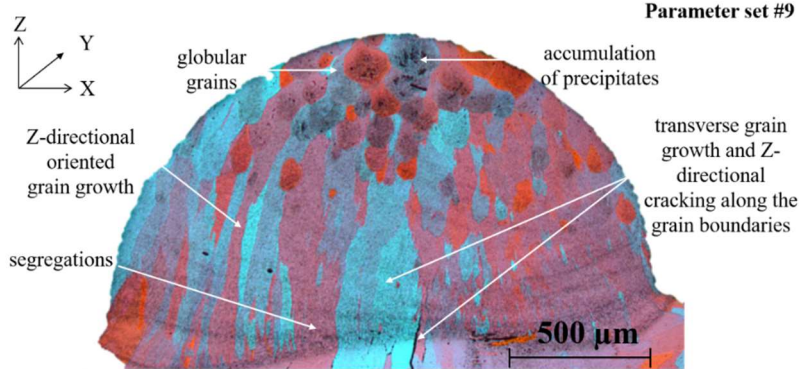


Fig. 10: Overview of the microstructural distribution within LMD processed beads and crack growth direction within a produced specimen using parameter set #9.

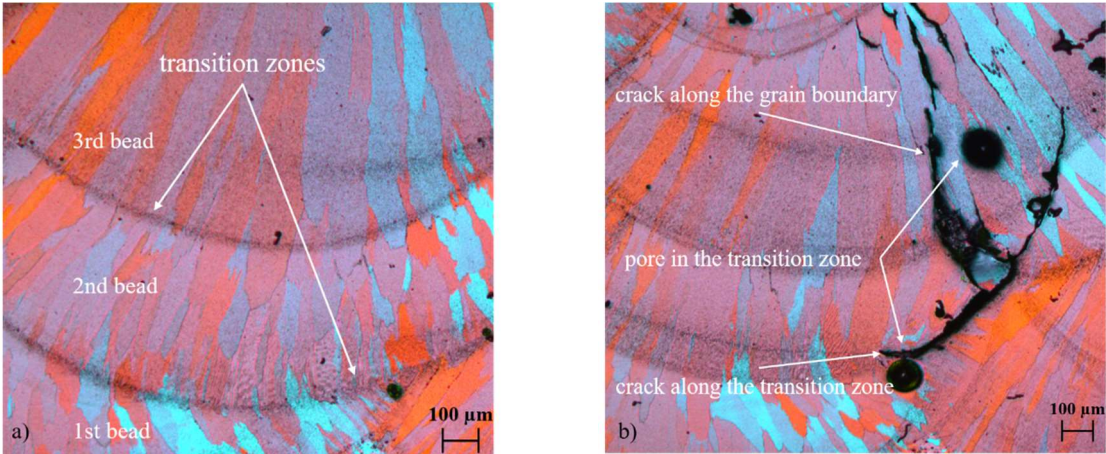


Fig. 11: Grain shape and Z-directional grain growth behavior (a), pore and crack occurrence and growth direction (b), in a structure deposited using parameter set #9.

Regarding the general behavior of the bead shaping relative to the chosen specific energy, Figs. 12 and 13 summarize the characteristics of bead height H , penetration depth h and bead width ω . It is pointed out, that the

aspect ratio R_B reduces by 35% with an increase of the energy density by 30%, from 128 J/g to 185 J/g. The ratio between bead height and penetration into the substrate material R_C shows a steep reduction of 45% with an increase of the afore mentioned magnitude of energy density. Concerning the dilution ratio derived from Equations (3.15) and (3.16), Fig. 13 shows an increase of 27%. Additionally, it is shown that Equation (3.16) could be used to determine this ratio in a simplified form. The deviation between these equations is 6%, which is in the range of the standard deviation of the measurements, therefore it is arguable to use Equation (3.16). As [47] already formulated, the bead side angle has to be large enough to avoid porosity, while overlapping individual tracks. Therefore, the side angle of the bead has also to be evaluated. The results plotted in Fig. 13 (b) show a decrease of 1° per 5 J/g. Summarizing, the range of the side angles lies between 36° to 47° . This decrease of the bead side angle is explained by the higher liquefaction of the material for higher energy inputs. The material does not form a Z-directional shape but increases in width and dilution of the bead, which can also be seen from Figs. 12 (a) and 13 (a). Generally, Figs. 12 and 13 show a similar trend showing that higher specific energies are favourable to develop flat structures of a high width in combination with a high penetration depth. This analysis allows to conclude that higher specific energies are favourable for surface coating and lower specific energies for structure building purposes.

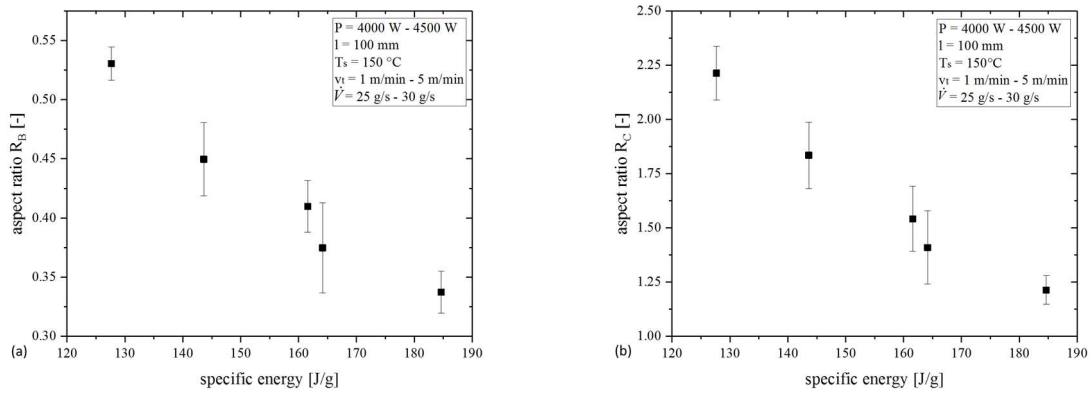


Fig. 12: Bead shape changes due to increased energies with respect to aspect ratio R_B (a) and dilution to deposition height ratio R_C (b).

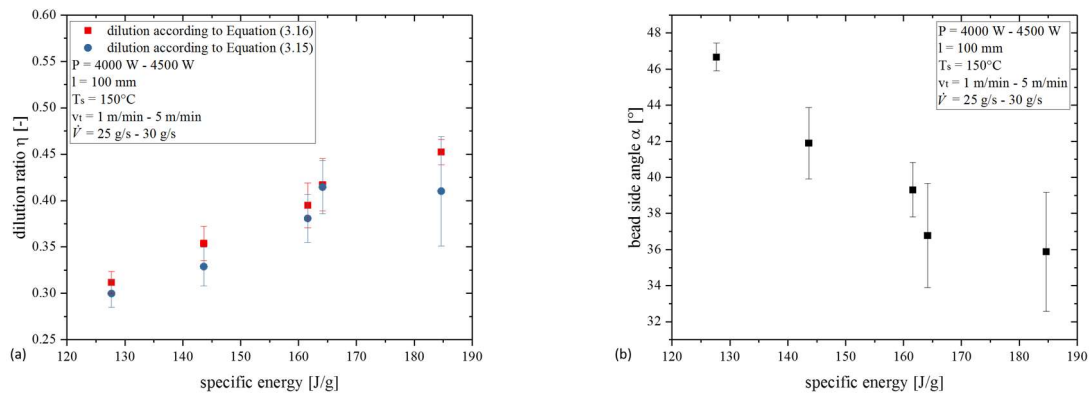


Fig. 13: Dilution η (a) and bead side angle α characteristics (b) for increased specific energies.

Using the identified parameters, two different bead shapes, depicted in Fig. 14, could be deposited using either higher or lower process energies. The general shape favourable to manufacture Z-directional structures is depicted in Fig. 14 (a). The shape of the upper part of the bead is similar to a top-hat distribution, which is advantageous for subsequent layer deposition. In order to process high-angled, Z-directional oriented beads, a process energy of 128 J/g was used. This leads to favourable characteristics for Z-directional structures with a bead side angle α of 46° and a dilution ratio η of 30%. A cross section of a manufactured bead using the indicated parameters is plotted in Fig. 14 (c).

By contrast, a low aspect ratio R_B and R_C connected with a high dilution rate are important factors in terms of a surface coating bead shaping. The general shape of a favourable bead in terms of surface coating processes is depicted in Fig. 14 (b). The shape of the upper part of the bead is similar to a gaussian distribution which is favourable for subsequent layer deposition next to it, leading to a good bonding and no surface defects. A parameter range including higher energy densities was identified. Using a value of 164 J/g, a low-angled and high diluted bead of 36° and 41% was manufactured. A cross section of a manufactured bead using the indicated parameters is plotted in Fig. 14 (d).

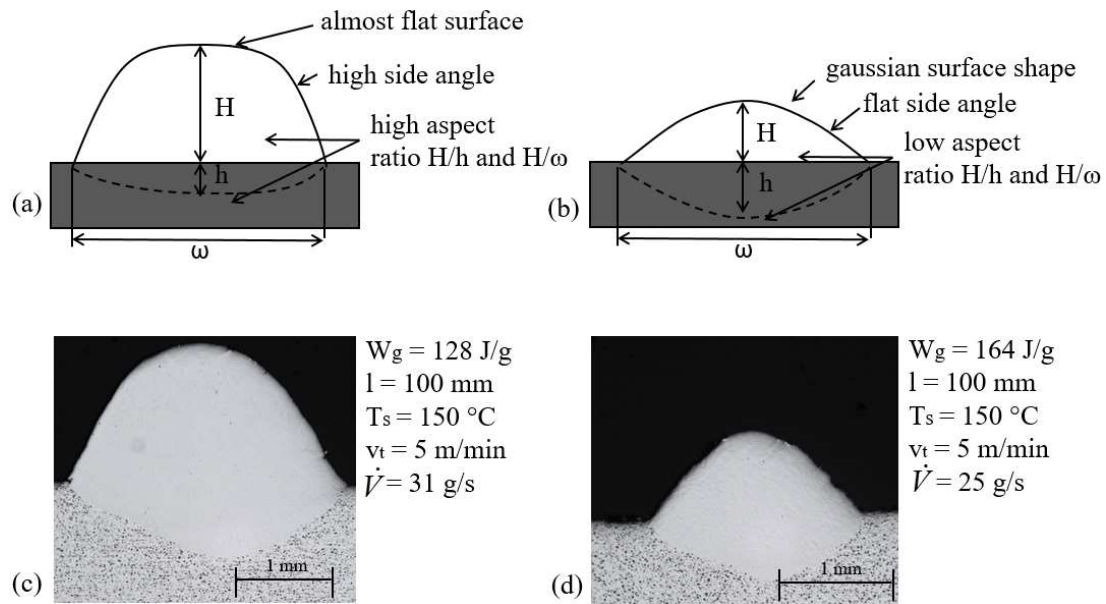


Fig. 14: Theoretical top hat-distribution (a) and gaussian-distribution (b) as well as cross sections of deposited beads showing top hat (c) and gaussian (d) shaped beads.

In order to get a smooth surface and a high X-directional deposition rate, the overlapping ratio μ_c and the optimum bead spacing d_c shown in Fig. 3 (b) has to be precisely determined. Considering Equations (3.9) – (3.14), the optimum bead spacing for substrate materials at 150°C and 300°C were calculated. Accordingly, process parameters leading to the bead shape depicted in Fig. 14 (b) have been chosen.

As a result of the geometric examinations of the beads, values of H and ω for the specific process parameters could be measured. Using these values in Equations (3.9) – (3.13), an optimum bead spacing of $d_c = 2.45$ mm in case of a pre-heated substrate of 150°C is calculated. According to Equation (3.14), this leads to an overlapping of $\mu_c = 18\%$. The surface shape of the conducted experiments for different bead spacings are shown in Fig. 15. A minimum roughness of $R_t = 0.13$ μm was achieved. A further decrease to a bead spacing of $d_c = 2.15$ mm did not improve the surface roughness. Hence, Fig. 15 (c) depicts the optimal bead spacing conditions for a pre-heated substrate of 150°C, choosing the afore identified parameters.

It was seen that the dilution increases for higher substrate temperatures, which is a positive effect for surface coating purposes. Additionally, it is assumed that the substrate temperature may overcome 150°C in multiple layer LMD. Therefore, the bead shape and optimization of bead spacing also for a pre-heated substrate at $T_s = 300^\circ\text{C}$ was analysed. Accordingly, Fig. 15 (e) – (h) show the results from a comparative study with a substrate temperature of 300°C. The increased substrate temperature led to an improvement of the surface quality. For this substrate temperature a bead spacing of $d_c = 2.8$ mm represents an optimum. These experimental results were supported by the theoretical considerations. As already mentioned a homogenous heat distribution is a very important factor in terms of process stability and reproducibility of constant bead shape quality. As a result of these investigations, workpieces, depicted in Fig. 16 (a), processed with a pre-heated substrate of $T_s = 300^\circ\text{C}$ and a coated surface area of 100 mm² were manufactured. A similar quality of each bead was achieved.

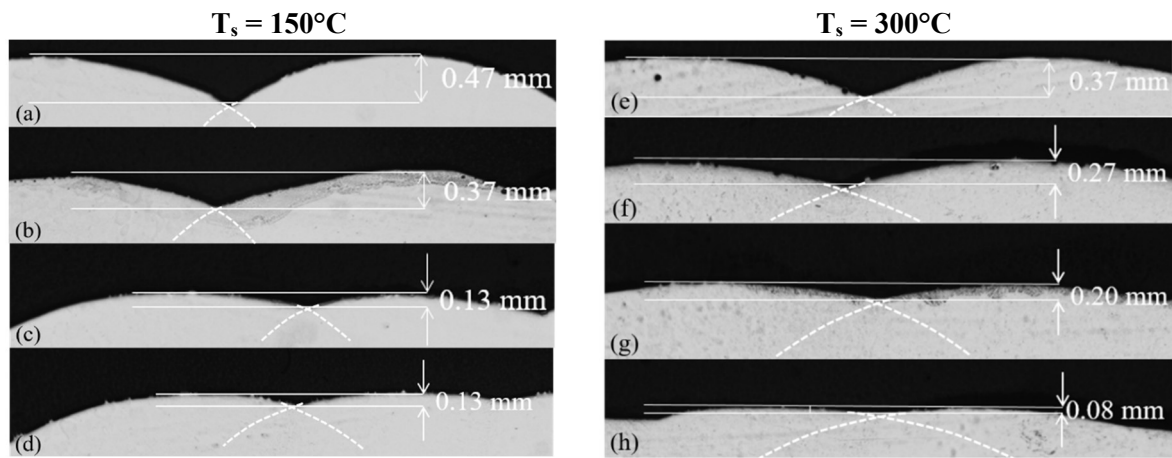


Fig. 15: Results from metallographic investigations concerning bead spacing of (a) $d_c = 3.4$ mm, (b) $d_c = 2.9$ mm, (c) $d_c = 2.45$ mm and (d) $d_c = 2.15$ mm for $T_s = 150^\circ\text{C}$ and bead spacings of (e) $d_c = 4.1$ mm, (f) $d_c = 3.6$ mm, (g) $d_c = 3.1$ mm and (h) $d_c = 2.8$ mm for $T_s = 300^\circ\text{C}$.

Equally important, a predictable process for structure building purposes needs to be developed. The objective of building Z-directional structures requires constantly low diluted, high angled and top-hat distributed bead shapes. Within the process, the wire was repositioned with a Z-directional distance $d_z = H$ to the before deposited bead after each deposition. In this study, constant parameters within one structure were used. Fig. 16 (b) shows a deposited wall consisting of 110 layers and a predicted single bead height of 1.8 mm. Indeed, the predicted height of the structure of 200 mm was not reached. Therefore, a method for prediction the height of the deposited structure was proposed. Metallographic analyses was used to get an insight into the structure. Using this approach it was possible to reveal the deposition height per deposited bead.

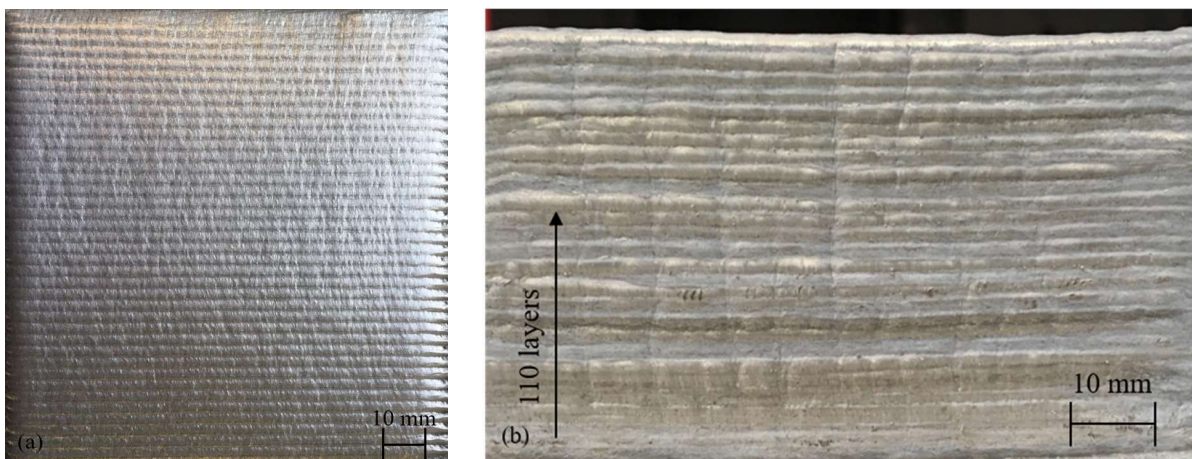


Fig. 16: A surface coating area of 100 mm^2 (a) and structure building of 110-layer deposition with a height of 50 mm (b)

Metallographic cross sections were used in order to reveal the deposition height within the structure. Fig. 17 visualizes a metallographic analyses of an 8-layer structure. Special attention was paid to identify the transition zones between the layers, the deposition height and the general grain growth behavior. Fig. 17 (a) reveals the deposition height inside the bead as uniformly distributed. The predicted bead height from single bead experiments is equal $H_1 = 1.8$ mm, whereas the predominant deposition height within the structure is $H_2 = 0.45$ mm. Assuming a bead height of 1.8 mm, the 8-layer structure should reach a height of 14.4 mm. Indeed the total height reaches only 5 mm. This is reasoned in a dilution in the formerly deposited bead which decreases the deposition height per

bead to $\sim 1/4$ of the predicted height. Regarding the post processing in terms of finishing the structure with a plane surface for application, the top of the structure has to be milled down by $1/3$ of the height of the last deposited bead. This is shown in Fig. 17 (b). Taking this into account the total height of the Z-directional structure can be calculated as

$$\frac{n - 1 \cdot H}{4} + H = H_{end}, \quad (5.1)$$

where n represents the number of beads and H is the predicted height of each bead according to the chosen parameter set¹. In Fig. 17 (b), the geometry of the post-processed structure as well as the general grain growth behavior are identified.

Special attention has also to be payed on the temperature distributions during the process. Due to different cooling rates in different regions of the structure characteristic microstructural features occur [48]. During the deposition of the first layers, the heat can easily proceed into the substrate and consequently flow into a large amount of surrounding material. Therefore, grain growth direction develops as a curvature near the substrate. This heat flow condition changes for each additional layer because the distance to the substrate increases and the cross sectional area for heat conduction reduces to the cross sectional area of the deposited structure. This leads to higher process temperatures in the center of the structure. It can be seen, that the Z-directional grain growth holds for the center of the bead as the temperature reach here its maximum. On the top surface of the structure the surrounding atmosphere cools down the material from all sides except from underneath. This leads again to a curved grain growth and globular grain shaping at the sides. The radius of the grains, located near the top surface was measured to be $r = 2.01$ mm, the center of the structure showed a grain radius of $r = 8.80$ mm. Consequently, mechanical properties in center and upper/lower areas are assumed to be different. In addition, in the top region of the structure accumulated precipitates occur. This is explained by heat accumulation in the structure, which leads to a reannealing during cooling.

These results provide important insights regarding the adaption of formerly specified process and parameter dependencies. Therefore, they constitute the framework to adapt necessary parameter in consideration of its specific aim, whether to coat or build structures.

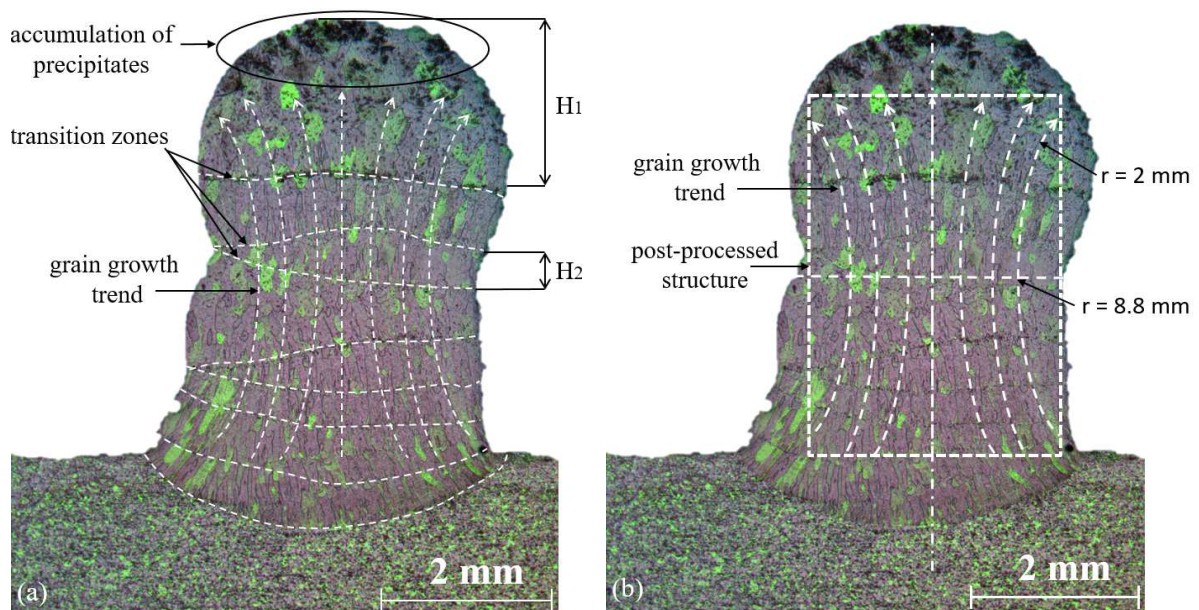


Fig. 17: Metallographic analyses concerning Z-directional LMD with special attention to identification of layer intersections (a) and grain growth behavior (b) within one structure.

¹ The total height of the 8-layer structure is calculated using Equation (5.1) to $(7 \cdot 1.8 \text{ mm})/4 + 1.8 \text{ mm} = 5 \text{ mm}$ and the height of the 110-layer wall can be calculated to $(109 \cdot 1.8 \text{ mm})/4 + 1.8 \text{ mm} = 51 \text{ mm}$.

6. Conclusions

Recent developments in the field of AM have led to a renewed interest in the investigation of processable materials. However, in terms of wire-based LMD there is a lack of knowledge regarding the possibility to process aluminium and its alloys. Within this study, a process for wire-based laser metal deposition of the AlMg alloys 5087 as wire and 5754 as substrate material was successfully set-up and investigated.

Important process effects and parameters were identified using a systematic parametric study. In the experiments, a strong dependency between the laser power and the deposition velocity as well as the deposition rate with respect to inner defects such as porosity was identified. Energy densities between $W_g = 125 \text{ J/g}$ to 185 J/g allow to achieve a density of the structure to more than $\rho_{bead} = 99.99\%$. The averaged pore size was calculated to $d_{pore} = 0.345 \text{ mm}$, additionally it was worked out that pore sizes between 0.24 mm and 0.48 mm occur with a probability of 68.2% . Regarding the localization of porosity, it was determined that large pores as well as its highest accumulation occurred in the start and end regions of the beads. In industrial application these regions have to be post-processed or excluded.

Regarding the shape of the deposited beads, one interesting finding is a strong dependency between specific process energy and bead geometry. High energies result in high diluted, broad expanded and low Z-directional deposited beads. The side angle of the beads decreases for higher energy densities. Taking this into account a subdivision between Z- and X-directional LMD process parameters is required. Whereas Z-directional structure building processes require low dilution and high deposition rates in terms of high profitable efficiency, X-directional coating processes require high bead widths and dilution rates. The perception that the aspect ratio R_B reduces by 35% and consequently the bead angle by 45% with an increase of the energy density of 30% was the driving fact to divide the two processes into coating and structure building process windows. In terms of surface coating strategies, an optimal bead spacing of $d_c = 2.45 \text{ mm}$ for $T_s = 150^\circ\text{C}$ and $d_c = 2.8 \text{ mm}$ for $T_s = 300^\circ\text{C}$ were identified. Using formerly identified coating parameters surface roughnesses for $T_s = 150^\circ\text{C}$ of $R_t = 0.13 \text{ }\mu\text{m}$ and $T_s = 300^\circ\text{C}$ of $R_t = 0.08 \text{ }\mu\text{m}$ before subsequent post-processing were possible to achieve. Concerning structure building, stable process conditions for defined parameter sets were developed and a method to predict the total height of the structure was illustrated.

Furthermore, grain growth direction was identified to be generally Z-directional and the shape of the grains to be longitudinal within the structure. In upper regions, the shape becomes globular, contenting a cluster of precipitates. Besides that, grain growth direction shows a curved gradient with increasing distance to the center of the structure. Regarding inner defects, porosity and cracks were frequently detected in the transition zones of the beads. It can be summarized that the wire-based laser metal deposition processability of the AlMg alloy 5087 could be successfully conducted.

Regarding temperature distributions, cooling rates and resulting features reasoned in heat transfer mechanisms only assumptions could be made. However, a different deposition rate and bead shape due to a pre-heated substrate is identified. More research using controlled temperature measurements are needed in order to identify temperature related effects and prove the formulated assumptions. Additionally, future research is required to investigate the detailed microstructure of the specimens, mechanical properties e.g. stress-strain behavior, microhardness, fatigue crack initiation and crack propagation. A further study could also assess residual stresses, expressed by distortional effects of the substrate.

Acknowledgements

The authors would like to thank Mr. R. Dinse, Mr. P. Haack and Mr. F. Dorn from Helmholtz-Zentrum Geesthacht for their valuable technical support.

7. References

- [1] S. W. Williams, F. Martina, A. C. Addison, J. Ding, G. Pardal, and P. Colegrove, "Wire + Arc Additive Manufacturing," *Mater. Sci. Technol.*, vol. 32, no. 7, pp. 641–647, May 2016.
<https://doi.org/10.1179/1743284715Y.0000000073>
- [2] J. Gu, B. Cong, J. Ding, S. W. Williams, and Y. Zhai, "Wire+Arc Additive Manufacturing of Aluminium," *SFF Symp. Austin, USA, Texas*, pp. 451–458, 2014.
- [3] W. U. H. Syed, A. J. Pinkerton, and L. Li, "A comparative study of wire feeding and powder feeding in direct diode laser deposition for rapid prototyping," *Appl. Surf. Sci.*, vol. 247, no. 1–4, pp. 268–276, 2005.
<https://doi.org/10.1016/j.apsusc.2005.01.138>
- [4] L. Dubourg and J. Archambeault, "Technological and scientific landscape of laser cladding process in 2007," *Surf. Coatings Technol.*, vol. 202, no. 24, pp. 5863–5869, 2008.
- [5] M. Karg, B. Ahuja, and M. Schmidt, "Processability of High Strength Aluminium-Copper Alloys AW-2022 and 2024 by Laser Beam Melting in Powder Bed," *Proc. 25th Solid Free. Fabr. Symp.*, pp. 420–436, 2014.
- [6] J. Fessler, R. Merz, A. Nickel, F. Prinz, and L. Weiss, "Laser deposition of metals for shape deposition manufacturing," *Solid Free. Fabr. Symp. Proceedings, Univ. Texas Austin, USA*, pp. 117–124, 1996.
<http://lov2ty04.free.fr/Projet/SMD.pdf>
- [7] F. Martina, J. Mehnen, S. W. Williams, P. Colegrove, and F. Wang, "Investigation of the benefits of plasma deposition for the additive layer manufacture of Ti-6Al-4V," *J. Mater. Process. Technol.*, vol. 212, no. 6, pp. 1377–1386, 2012.
<https://doi.org/10.1016/j.jmatprotec.2012.02.002>
- [8] S. N. Grigoriev, T. V. Tarasova, G. O. Gvozdeva, and S. Nowotny, "Structure Formation of Hypereutectic Al-Si-Alloys Produced by Laser Surface Treatment," *J. Mech. Eng.*, vol. 60, no. 6, pp. 389–394, 2014.
<https://doi.org/10.5545/sv-jme.2013.1211>
- [9] E. O. Olakanmi, R. F. Cochrane, and K. W. Dalgarno, "A review on selective laser sintering/melting (SLS/SLM) of aluminium alloy powders: Processing, microstructure, and properties," *Prog. Mater. Sci.*, vol. 74, pp. 401–477, 2015.
<https://doi.org/10.1016/j.pmatsci.2015.03.002>
- [10] T. E. Abioye, J. Folkes, and A. T. Clare, "A parametric study of Inconel 625 wire laser deposition," *J. Mater. Process. Technol.*, vol. 213, no. 12, pp. 2145–2151, 2013.
<https://doi.org/10.1016/j.jmatprotec.2013.06.007>
- [11] P. Kazanas, P. Deherkar, P. Almeida, H. Lockett, and S. Williams, "Fabrication of geometrical features using wire and arc additive manufacture," *Proc. Inst. Mech. Eng. Part B J. Eng. Manuf.*, vol. 226, no. 6, pp. 1042–1051, 2012.
<https://doi.org/10.1177/0954405412437126>
- [12] Y. P. Kathuria, "Some aspects of laser surface cladding in the turbine industry," *Surf. Coatings Technol.*, vol. 132, no. 2–3, pp. 262–269, 2000.
[https://doi.org/10.1016/S0257-8972\(00\)00735-0](https://doi.org/10.1016/S0257-8972(00)00735-0)
- [13] W. E. Frazier, "Metal additive manufacturing: A review," *J. Mater. Eng. Perform.*, vol. 23, no. 6, pp. 1917–1928, 2014.
<https://doi.org/10.1007/s11665-014-0958-z>
- [14] N. Kang, P. Coddet, C. Chen, Y. Wang, H. Liao, and C. Coddet, "Microstructure and wear behavior of in-situ hypereutectic Al-high Si alloys produced by selective laser melting," *Mater. Des.*, vol. 99, pp. 120–126, 2016.
<http://dx.doi.org/10.1016/j.matdes.2016.03.053>

- [15] W. U. H. Syed and L. Li, "Effects of wire feeding direction and location in multiple layer diode laser direct metal deposition," *Appl. Surf. Sci.*, vol. 248, no. 1–4, pp. 518–524, 2005.
<https://doi.org/10.1016/j.apsusc.2005.03.039>
- [16] F. Weng, C. Chen, and H. Yu, "Research status of laser cladding on titanium and its alloys: A review," *Mater. Des.*, vol. 58, no. 2016, pp. 412–425, 2014.
<http://dx.doi.org/10.1016/j.optlaseng.2017.02.007>
- [17] Y. Huang, "Characterization of dilution action in laser-induction hybrid cladding," *Opt. Laser Technol.*, vol. 43, no. 5, pp. 965–973, 2011.
<https://doi.org/10.1016/j.optlastec.2010.12.005>
- [18] S. Nowotny, S. Scharek, E. Beyer, and K. H. Richter, "Laser beam build-up welding: Precision in repair, surface cladding, and direct 3D metal deposition," *J. Therm. Spray Technol.*, vol. 16, no. 3, pp. 344–348, 2007.
<https://doi.org/10.1007/s11666-007-9028->
- [19] S. W. Huang, M. Samandi, and M. Brandt, "Abrasive wear performance and microstructure of laser clad WC/Ni layers," *Wear*, vol. 256, no. 11–12, pp. 1095–1105, 2004.
[https://doi.org/10.1016/S0043-1648\(03\)00526-X](https://doi.org/10.1016/S0043-1648(03)00526-X)
- [20] J. Yan, X. Zeng, M. Gao, J. Lai, and T. Lin, "Effect of welding wires on microstructure and mechanical properties of 2A12 aluminum alloy in CO₂ laser-MIG hybrid welding," *Appl. Surf. Sci.*, vol. 255, no. 16, pp. 7307–7313, 2009.
<https://doi.org/10.1016/j.apsusc.2009.03.088>
- [21] M. Froend *et al.*, "Fiber laser welding of dissimilar titanium (Ti-6Al-4V / cp-Ti) T-joints and their laser forming process for aircraft application," *Opt. Laser Technol.*, vol. 96, pp. 123–131, 2017.
<https://doi.org/10.1016/j.optlastec.2017.05.017>
- [22] J. Ding *et al.*, "Thermo-mechanical analysis of Wire and Arc Additive Layer Manufacturing process on large multi-layer parts," *Comput. Mater. Sci.*, vol. 50, no. 12, pp. 3315–3322, 2011.
<https://doi.org/10.1016/j.commatsci.2011.06.023>
- [23] Y. Shi, Y. Liu, P. Yi, and J. Hu, "Effect of different heating methods on deformation of metal plate under upsetting mechanism in laser forming," *Opt. Laser Technol.*, vol. 44, no. 2, pp. 486–491, 2012.
<https://doi.org/10.1016/j.optlastec.2011.08.019>
- [24] P. Mercelis and J.-P. Kruth, "Residual stresses in selective laser sintering and selective laser melting," *Rapid Prototyp. J.*, vol. 12, no. 5, pp. 254–265, 2006.
<https://doi.org/10.1108/13552540610707013>
- [25] P. Vora, K. Mumtaz, I. Todd, and N. Hopkinson, "AlSi12 in-situ alloy formation and residual stress reduction using anchorless selective laser melting," *Addit. Manuf.*, vol. 7, pp. 12–19, 2015.
<https://doi.org/10.1016/j.addma.2015.06.003>
- [26] P. A. Colegrove *et al.*, "Microstructure and residual stress improvement in wire and arc additively manufactured parts through high-pressure rolling," *J. Mater. Process. Technol.*, vol. 213, no. 10, pp. 1782–1791, 2013.
<https://doi.org/10.1016/j.jmatprotec.2013.04.012>
- [27] N. Contuzzi, S. L. Campanelli, and A. D. Ludovico, "3D finite element analysis in the selective laser melting process," *Int. J. Simul. Model.*, vol. 10, no. 3, pp. 113–121, 2011.
[https://doi.org/10.2507/IJSIMM10\(3\)1.169](https://doi.org/10.2507/IJSIMM10(3)1.169)
- [28] B. A. Szost *et al.*, "A comparative study of additive manufacturing techniques : Residual stress and microstructural analysis of CLAD and WAAM printed Ti – 6Al – 4V components," *Mater. Des.*, vol. 89, pp. 559–567, 2016.
<https://doi.org/10.1016/j.matdes.2015.09.115>

- [29] I. N. Maliutina *et al.*, “Laser Cladding of Gamma-TiAl Intermetallic Alloy on Titanium Alloy Substrates,” *Metall. Mater. Trans. A Phys. Metall. Mater. Sci.*, vol. 47, no. 1, pp. 378–387, 2015.
<https://doi.org/10.1007/s11661-015-3205-9>
- [30] J. Xu, W. Liu, Y. Kan, and M. Zhong, “Microstructure and wear properties of laser cladding Ti–Al–Fe–B coatings on AA2024 aluminum alloy,” *Mater. Des.*, vol. 27, no. 5, pp. 405–410, 2006.
<http://dx.doi.org/10.1016/j.optlaseng.2009.08.003>
- [31] B. Carcel, J. Sampedro, A. Ruescas, and X. Toneu, “Corrosion and wear resistance improvement of magnesium alloys by laser cladding with Al–Si,” *Phys. Procedia*, vol. 12, no. PART 1, pp. 353–363, 2011.
<https://doi.org/10.1016/j.phpro.2011.03.045>
- [32] L. Dubourg, D. Ursescu, F. Hlawka, and A. Cornet, “Laser cladding of MMC coatings on aluminium substrate: Influence of composition and microstructure on mechanical properties,” *Wear*, vol. 258, no. 11–12, pp. 1745–1754, 2005.
<https://doi.org/10.1016/j.wear.2004.12.010>
- [33] X. Cao, M. Jahazi, J. Fournier, and M. Alain, “Optimization of bead spacing during laser cladding of ZE41A-T5 magnesium alloy castings,” *J. Mater. Process. Technol.*, vol. 205, no. 1–3, pp. 322–331, 2008.
<https://doi.org/10.1016/j.jmatprotec.2007.11.120>
- [34] E. Toyserkani, A. Khajepour, and S. Corbin, “Laser Cladding,” *CRC Press. Boca Raton, London, New York, Washingt. D.C.*, p. 280, 2005.
- [35] K. Zhang, S. Wang, W. Liu, and X. Shang, “Characterization of stainless steel parts by Laser Metal Deposition Shaping,” *Mater. Des.*, vol. 55, pp. 104–119, 2014.
<https://doi.org/10.1016/j.matdes.2013.09.006>
- [36] K. Zhang, X. M. Zhang, and W. J. Liu, “Influences of Processing Parameters on Dilution Ratio of Laser Cladding Layer during Laser Metal Deposition Shaping,” *Adv. Mater. Res.*, vol. 549, no. 1, pp. 785–789, 2012.
<https://doi.org/10.4028/www.scientific.net/AMR.549.785>
- [37] R. Cottam, V. Luzin, Q. Liu, Y. C. Wong, J. Wang, and M. Brandt, “Investigation into Heat Treatment and Residual Stress in Laser Clad AA7075 Powder on AA7075 Substrate,” *Metallogr. Microstruct. Anal.*, vol. 2, no. 4, pp. 205–212, 2013.
<https://doi.org/10.1007/s13632-013-0080-x>
- [38] M. Shiomi, K. Osakada, K. Nakamura, T. Yamashita, and F. Abe, “Residual Stress within Metallic Model Made by Selective Laser Melting Process,” *CIRP Ann. - Manuf. Technol.*, vol. 53, no. 1, pp. 195–198, 2004.
[https://doi.org/10.1016/S0007-8506\(07\)60677-5](https://doi.org/10.1016/S0007-8506(07)60677-5)
- [39] F. Abe, K. Osakada, M. Shiomi, K. Uematsu, and M. Matsumoto, “The manufacturing of hard tools from metallic powders by selective laser melting,” *J. Mater. Process. Technol.*, vol. 111, no. 1–3, pp. 210–213, 2001.
[https://doi.org/10.1016/S0924-0136\(01\)00522-2](https://doi.org/10.1016/S0924-0136(01)00522-2)
- [40] K. Senthilkumaran, P. M. Pandey, and P. V. M. Rao, “Influence of building strategies on the accuracy of parts in selective laser sintering,” *Mater. Des.*, vol. 30, no. 8, pp. 2946–2954, 2009.
<http://dx.doi.org/10.1016/j.matdes.2009.01.009>
- [41] H. Jung, “A Study on Laser Forming Processes with Finite Element Analysis,” *Dr. thesis, Univ. Canterbury, New Zeal.*, 2006.
<https://doi.org/http://hdl.handle.net/10092/1099>
- [42] F. Vollertsen and M. Rodle, “Model for the temperature gradient mechanism of laser bending,” *Proc. LANE*, pp. 371–378, 1994.

- [43] W. U. H. Syed, A. J. Pinkerton, and L. Li, "Combining wire and coaxial powder feeding in laser direct metal deposition for rapid prototyping," *Appl. Surf. Sci.*, vol. 252, no. 13, pp. 4803–4808, 2006.
<https://doi.org/10.1016/j.apsusc.2005.08.118>
- [44] J. Huang, Z. Li, H. Cui, C. Yao, and Y. Wu, "Laser welding and laser cladding of high performance materials," *Phys. Procedia*, vol. 5, no. PART 2, pp. 1–8, 2010.
<https://doi.org/10.1016/j.phpro.2010.08.023>
- [45] Y. Chen *et al.*, "Investigation of dendritic growth and liquation cracking in laser melting deposited Inconel 718 at different laser input angles," *Mater. Des.*, vol. 105, pp. 133–141, 2016.
<http://dx.doi.org/10.1016/j.matdes.2016.05.034>
- [46] M. Sergio, F. De Lima, and S. Sankaré, "Microstructure and mechanical behavior of laser additive manufactured AISI 316 stainless steel stringers," *Mater. Des.*, vol. 55, pp. 526–532, 2014.
<http://dx.doi.org/10.1016/j.matdes.2013.10.016>
- [47] U. de Oliveira, V. Ocelík, and J. T. M. De Hosson, "Analysis of coaxial laser cladding processing conditions," *Surf. Coatings Technol.*, vol. 197, no. 2–3, pp. 127–136, 2005.
- [48] H. Tran *et al.*, "3D thermal finite element analysis of laser cladding processed Ti-6Al-4V part with microstructural correlations," *Mater. Des.*, vol. 128, no. April, pp. 130–142, 2017.
<http://dx.doi.org/10.1016/j.matdes.2017.04.092>